Title	Controlled CVD growth of Cu–Sb alloy nanostructures
Author(s)	Chen, Jing; Yin, Zongyou; Sim, Daohao; Tay, Yee Yan; Zhang, Hua; Ma, Jan; Hng, Huey Hoon; Yan, Qingyu
Citation	Chen, J., Yin, Z., Sim, D., Tay, Y. Y., Zhang, H., Ma, J., et al. (2011). Controlled CVD growth of Cu–Sb alloy nanostructures. Nanotechnology, 22(32).
Date	2011
URL	http://hdl.handle.net/10220/8279
Rights	© IOP Publishing Ltd. This is the author created version of a work that has been peer reviewed and accepted for publication by Nanotechnology, IOP Publishing Ltd. It incorporates referee's comments but changes resulting from the publishing process, such as copyediting, structural formatting, may not be reflected in this document. The published version is available at: [DOI: http://dx.doi.org/10.1088/0957-4484/22/32/325602]

Controlled CVD growth of Cu–Sb alloy nanostructures

Jing Chen, Zongyou Yin, Daohao Sim, Yee Yan Tay, Hua Zhang, Jan Ma, Huey Hoon Hng and Qingyu Yan[1]

School of Materials Science and Engineering, Nanyang Technological University, 50 Nanyang Avenue, Singapore 639798, Singapore

E-mail: alexyan@ntu.edu.sg

[1] *Author to whom any correspondence should be addressed.*

Abstract

Sb based alloy nanostructures have attracted much attention due to their many promising applications, e.g. as battery electrodes, thermoelectric materials and magnetic semiconductors. In many cases, these applications require controlled growth of Sb based alloys with desired sizes and shapes to achieve enhanced performance. Here, we report a flexible catalyst-free chemical vapor deposition (CVD) process to prepare Cu–Sb nanostructures with tunable shapes (e.g. nanowires and nanoparticles) by transporting Sb vapor to react with copper foils, which also serve as the substrate. By simply controlling the substrate temperature and distance, various Sb–Cu alloy nanostructures, e.g. $Cu_{11}Sb_3$ nanowires (NWs), Cu_2Sb nanoparticles (NPs), or pure Sb nanoplates, were obtained. We also found that the growth of $Cu_{11}Sb_3$ NWs in such a catalyst-free CVD process was dependent on the substrate surface roughness. For example, smooth Cu foils could not lead to the growth of $Cu_{11}Sb_3$ nanowires while roughening these smooth Cu foils with rough sand papers could result in the growth of $Cu_{11}Sb_3$ nanowires. The effects of gas flow rate on the size and morphology of the Cu–Sb alloy nanostructures were also investigated. Such a flexible growth strategy could be of practical interest as the growth of some Sb based alloy nanostructures by CVD may not be easy due to the large difference between the condensation temperature of Sb and the other element, e.g. Cu or Co.

S Online supplementary data available from stacks.iop.org/Nano/22/325602/mmedia

---

1. Introduction

Sb based alloys have attracted much attention due to their wide applications, such as for infrared imaging [1], as thermoelectric materials [2–4], magnetic materials [5, 6], and electrode materials for Li ion batteries [7–11]. In many case, these applications require controlled growth of Sb based alloys with desired sizes and shapes to achieve enhanced performance. Several approaches have been developed to synthesize nanostructured Sb alloys, e.g. ball milling [12, 13], electrochemical deposition [9, 14], solvothermal/hydrothermal process [15, 16], and catalyzed vapor–liquid–solid (VLS) growth [17, 18]. Electrochemical deposition can produce nanowire arrays with pre-defined size by using anodized aluminum oxide (AAO) templates, which may need to be removed before sample testing [19]. For the solvothermal/hydrothermal process, controlled synthesis of Sb and Sb based alloy nanocrystals remains a significant challenge due to the lack of suitable surfactants that can interact effectively with Sb. Sb displays high diffusivity and low surface energy [20, 21]; thus, during nanocrystal growth, Sb can easily diffuse onto the surface of the material and reduce the total surface energy as demonstrated in the molecular beam

epitaxial growth process [22]. Without effective functional groups to inhibit growth, the particle size and uniformity of the materials are difficult to control, and agglomeration can occur.

Catalyzed CVD growth is an effective process to grow nanowires (NWs) with aligned directions [17, 18]. However, the growth process sometimes can be limited by the physical properties of the individual elements, e.g. the vaporization temperature and condensation temperature. For example, Sb has a relatively low vaporization temperature of ~773 K. It is normally easy to grow samples of Sb alloyed with elements that have vaporization temperatures in the same range, e.g. In [17], Bi [23], Te [4, 24], etc. The process will be much more difficult for growing samples of Sb alloyed with elements that have high vaporization temperatures, e.g. Co (~1773 K) or Cu (~1473 K). The co-condensation region of both Sb and Co/Cu in the VLS furnace is limited, which makes the process very difficult to control. So far, to the best of our knowledge, there has been no report on the growth of nanowires of Co–Sb or Cu–Sb alloys by the CVD process.

Herein, we report a flexible catalyst-free CVD process to prepare Cu–Sb nanostructures, e.g. NWs or nanoparticles (NPs). During this growth process, we used Cu foils as both the Cu source and as substrates in the downstream position, to react with the Sb vapor condensed onto them. The morphology, phase, and size of the nanostructures could be tuned by varying the substrate distances and the Ar/H_2 gas flow rate. It was also found that the Cu–Sb alloy nanowires' growth is directly related to the surface roughness of the Cu substrates. For example, smooth Cu foils could not lead to the growth of the nanowires while roughening these smooth Cu foils with rough sand papers could result in the growth of nanowires. Such a growth strategy of the Cu–Sb alloy nanostructures can also be considered to extend to other Sb based alloys, e.g. Co–Sb or Fe–Sb etc.

2. Experimental details

The experiment was carried out in a horizontal tube furnace (Lindberg/Blue M). Sb powder (Sigma-Aldrich, 99.5%, 100 mesh) was used as-received. Copper foils with a size of 1 cm ×1 cm were carefully washed using ethanol and DI water and then dried. Sb powder was placed in the center of the tube furnace and two pieces of copper foil were placed at the 14 and 16 cm downstream side of the Sb powder. Before the experiment, the quartz tube with diameter of 1 in was evacuated to 10^{-3} mbar and then flushed with 95% Ar + 5% H_2 gas three times to prevent oxidation. The furnace was heated to 773 K at a heating rate of 30 K min^{-1} and kept there for 1 h. During the experiment, the flow rate of 95% Ar + 5% H_2 gas was controlled at 200 sccm (standard cubic centimeter per minute) by a mass flow meter controller. The pressure in the quartz tube was kept at 1.5 mbar by regulating the pump speed of the mechanical pump.

The $Cu_{11}Sb_3$ nanowires and Cu_2Sb nanoparticles on copper foils were directly used for scanning electron microscopy (SEM) and x-ray diffraction (XRD) measurements. For transmission electron microscopy (TEM) characterization, the copper foil was put into a small ampule. Then ethanol was added until it covered the surface of the substrate. After ultrasonicating for 1 h, the solution was dropped onto carbon coated 200 mesh nickel grids. The x-ray diffractograms were obtained using a Scintag PAD-V diffractometer with a Cu Kα irradiation. The size and morphology of the particles were characterized using field-emission SEM (JEOL JSM7600F) operating at 5 kV. Energy-dispersive x-ray analysis (EDX), high-resolution TEM (HRTEM), and selected area electron diffraction (SAED) were obtained by using a TEM JEOL 2100 system operating at 200 kV.

The $Cu_{11}Sb_3$ nanowire field effect transistor (FET) was fabricated. Firstly, the Au electrode pads were deposited on SiO_2/Si substrate through photolithography. Then, the $Cu_{11}Sb_3$ nanowires were peeled from the original support substrate and were dissolved into pure ethanol. After that, the solution was properly sonicated. The nanowire solution was carefully drop-cast onto the Au-pads area of the SiO_2/Si substrate followed by a drying process at 323 K for 1 h to form the final Cu– Sb nanowire FET devices. Then, the as-fabricated Cu–Sb nanowire FET was tested directly under ambient conditions.

3. Results and discussion

A typical synthesis was carried out by placing a crucible containing Sb powder in the center of the quartz tube that was heated at 773 K under continuous Ar/H_2 gas flow to transfer the Sb vapors to be deposited onto the Cu foil substrates set in the downstream positions. The temperature profile of the furnace is given in the supporting information (see supporting information figure S1 available at stacks.iop.org/ Nano/22/325602/mmedia). It was revealed by the SEM and TEM images (see figures 1(a) and (b)) that straight NWs were grown on the Cu foils at a substrate distance of d_{sub} = 14 cm from the center of the tube furnace with the Ar/H_2 gas flow rate $F_{Ar/H2}$ = 200 sccm. These NWs are 100–200 nm in diameter and 2 μm in length. The EDX measurement in the TEM (see supporting information figure S2 available at stacks. iop.org/Nano/22/325602/mmedia) on these NWs showed the atomic ratio of Cu:Sb = 11:3. Here, nickel grids were used to support the NWs for the TEM and HRTEM observation. The SAED on a nanowire showed a spot diffraction pattern (see figure 1(c)) corresponding to the orthorhombic $Cu_{11}Sb_3$ phase (JCPDS card 042-0823) and also indicated the single crystalline nature of the NWs. The HRTEM image (figure 1(d)) shows a lattice spacing of 0.216 nm along the long axis of the NW, which indicates the NW grew along the (002) lattice direction. The x-ray diffraction pattern of these NWs (see figure 1(e)) shows only diffraction peaks corresponding to the orthorhombic $Cu_{11}Sb_3$ and Cu foils. No additional peaks from impurity phases were detected.

In order to further understand the growth process of the $Cu_{11}Sb_3$ NWs, we carried out the experiment on two different Cu substrates. As examined from the SEM image (see supporting information figure S3a available at stacks.iop.org/Nano/22/325602/mmedia), the Cu foils used for the above NW's growth were relatively rough with an average surface roughness (Ra) of 154 nm (see supporting information figure S3b available at stacks. iop.org/Nano/22/325602/mmedia). Replacing the rough substrates with a relatively smooth Cu foil (see supporting information figure S3c available at stacks.iop.org/Nano/22/325602/mmedia), with an average surface roughness (Ra) of 66 nm (see supporting information figure S3d available at stacks.iop.org/Nano/22/325602/mmedia), resulted in the growth of clustered particles (see figure 2(a)) instead of NWs. The size of the as-grown particles was in the range of 0.5–2 μm without any change of the composition and phase (see supporting information figure S4 available at stacks.iop.org/Nano/22/325602/mmedia). However, if we roughened the smooth Cu foils with P800 sand paper and annealed them at 563 K under Ar atmosphere for 30 min, the Cu foils became rougher with an average surface roughness (Ra) of 212 nm (see supporting information figure S3e and f available at stacks.iop. org/Nano/22/325602/mmedia). Then, under the same growth conditions, $Cu_{11}Sb_3$ NWs were successfully grown using these roughened Cu foils (see figure 2(b)). Based on the above observation, we concluded that the surface convex on the rough Cu foil surface served as the seeds or the catalysts to initiate the growth of $Cu_{11}Sb_3$ NWs in such a CVD process. The Cu foils also provided the Cu source to react with the Sb vapor deposited on it at elevated substrate temperature, e.g. ~563 K.

The growth of the $Cu_{11}Sb_3$ NWs under different flow rates was also investigated. It was shown

that decreasing the Ar/H_2 gas flow rate ($F_{Ar/H2}$) led to the growth of NWs with shorter lengths and larger diameters (see figure 3(a)) for the same growth time t_g. For example, decreasing $F_{Ar/H2}$ from 200 to 100 sccm resulted in the growth of NWs with an average length of 1.5 μm and an average diameter of 500 nm for t_g = 1 h. Further decreasing $F_{Ar/H2}$ to 50 sccm, we found that the as-grown NWs for t_g = 1 h were even shorter, with an average length of 1 μm and diameter above 1 μm, and were also partially agglomerated (see figure 3(b)). The growth of the NWs could be considered as a competing process between the nucleation/growth and the surface diffusion of the as-deposited atoms. Lower gas flow rates slow down the transport of the Sb vapor to the substrates and led to a slower nucleation/growth process. As the deposition process slows down, the as-deposited atoms are allowed to have more time to diffuse along the surface of the substrate before the next layered atoms are deposited. The diffusion of the as-deposited atoms leads to the increase in the NW diameter.

Decreasing the substrate temperature to ~503 K by increasing d_{sub} to 16 cm led to the growth of nanoparticles (NPs) as shown by the SEM and TEM images (see figures 4(a) and (b)). The growth of NPs was not dependent on the types of Cu foils used. The size of the particles could be tuned by adjusting $F_{Ar/H2}$, e.g. the average size was ~200 nm for $F_{Ar/H2}$ = 200 sccm, and ~1 μm for $F_{Ar/H2}$ = 50 sccm (see figure 4(c)). The larger size obtained for the NPs was also attributed to the surface diffusion of the as-deposited atoms along the substrate surface and the slower nucleation/growth process. The EDX analysis in the TEM revealed that the atomic ratio of the particles was Cu:Sb = 2:1. The spot pattern revealed by the SAED (see figure 4(d)) indicates that the NPs were single crystalline tetragonal Cu_2Sb (JCPDS card 003-1023), which is consistent with the HRTEM observation (see figure 4(e)). No additional peaks from the impurity phase were observed in the XRD pattern of the Cu_2Sb nanoparticle samples (see figure 4(f)). Unlike the growth of the $Cu_{11}Sb_3$ NWs, the substrate temperature for the Cu_2Sb NPs was lower, which limited the amount of Cu to react with the Sb vapor. The resulting tetragonal Cu_2Sb did not show preferred growth along any particular lattice direction.

Further decreasing the substrate temperature to 353 K by increasing d_{sub} to 20 cm resulted in the growth of nanoplates (see figures 5(a) and (b)). These nanoplates were 150– 200 nm in diameter with thickness of 8–15 nm. The EDX analysis (see supporting information figure S5 available at stacks.iop.org/Nano/22/325602/mmedia) in the TEM showed only the presence of Sb. The spot pattern revealed by the SAED (see figure 5(c)) shows that these nanoplates are single crystalline rhombohedral Sb (JCPDS card 035-0732). This observation suggested that the reaction between the Cu from the substrate and the Sb vapor is highly dependent on the substrate temperature. Decreasing the substrate temperature resulted in less Cu content in the as-grown samples. At d_{sub} > 18 cm with a substrate temperature of 433 K, no Cu reacted with the Sb vapor to form the Cu–Sb alloys. The HRTEM observation indicated that these single crystalline Sb nanoplates showed (110) facets along their main surface (see figure 5(d)), which was mainly due to the confined growth within the (001) planes. The morphology of these Sb nanocrystals can be tuned by changing the substrate distance. Further increasing d_{sub} to 25 cm resulted in the growth of Sb nanoplates with smaller diameters, e.g. 80–100 nm, and thinner thicknesses, e.g. ~6 nm (see figure 5(e)). The XRD patterns also confirmed that there was no impurity phase in the nanoplates grown at both substrate distances except for the rhombohedral Sb phase (see figure 5(f)).

We also investigated the electrical transport property of the $Cu_{11}Sb_3$ NWs by field effect measurements on single $Cu_{11}Sb_3$ NW. The field effect device, shown in the supporting information figure S6 (available at stacks.iop.org/Nano/22/325602/mmedia), is a back-gate device. Figure 6(a) shows the typical source–drain current (I_{ds}) versus voltage (V_{ds}) curves with different

gate voltages (V_g) ranging from 0 to 30 V. The linear shapes indicated ohmic contacts between the Au electrodes and $Cu_{11}Sb_3$ NW. The increased I_{ds} values with increasing V_{gs} behavior (see figure 6(b)) suggested that the $Cu_{11}Sb_3$ NW showed n-type semiconductor characteristics. The total resistance of the device can be calculated from the I_{ds} versus V_{ds} curve at V_g = 0 V (see figure 6(a)), that is 78 MΩ. The contact resistances may contribute to such high resistance [25].

4. Conclusion

In summary, we used a simple catalyst-free CVD process to grow Cu–Sb alloy nanostructures by having the Cu foils acting as both the substrates and the Cu source. Due to the large difference in the condensation temperatures of Cu vapor and Sb vapor, co-condensation of Cu and Sb vapors is difficult to control. Using Cu foils as the substrates and the Cu source in such a CVD process offers a simple and flexible route to prepare Cu–Sb alloy nanostructures, in which the morphology, size, and phases can be tuned by various parameters. Cu– Sb alloy NWs and NPs with varied shapes, sizes, and phases were prepared by varying the substrate surface roughness, the substrate temperature, and the flow rates. Sb nanoplates with controlled size were synthesized at longer substrate distances. Such a growth strategy can be extended to other Sb alloys when the condensation temperatures of the elements are greatly different, e.g. Co–Sb.

Acknowledgments

The authors gratefully acknowledge AcRF Tier 1 RG 31/08 of MOE (Singapore), NRF2009EWT-CERP001-026 (Singapore), and AcRF Tier 2 (ARC 7/10, No. MOE2010-T2-1-017). HZ is grateful for the support of AcRF Tier 2 (ARC 10/10, No. MOE2010-T2-1-060) from MOE in Singapore.

References

[1] Norton P R 1991 Infrared image sensors *Opt. Eng.* **30** 1649–63

[2] Caillat T, Fleurial J P and Borshchevsky A 1997 Preparation and thermoelectric properties of semiconducting Zn_4Sb_3 *J. Phys. Chem. Solids* **58** 1119–25

[3] Yang L, Hng H H, Li D, Yan Q Y, Ma J, Zhu T J, Zhao X B and Huang H 2009 Thermoelectric properties of p-type $CoSb_3$ nanocomposites with dispersed $CoSb_3$ nanoparticles *J. Appl. Phys.* **106** 6

[4] Chen J *et al* 2010 Sb_2Te_3 nanoparticles with enhanced Seebeck coefficient and low thermal conductivity *Chem. Mater.* **22** 3086–92

[5] Hu R W *et al* 2008 Colossal positive magnetoresistance in a doped nearly magnetic semiconductor *Phys. Rev.* B **77** 5

[6] Ravindran P, Delin A, James P, Johansson B, Wills J M, Ahuja R and Eriksson O 1999 Magnetic, optical, and magneto-optical properties of MnX (X = As, Sb, or Bi) from full-potential calculations *Phys. Rev.* B **59** 15680–93

[7] Wachtler M, Winter M and Besenhard J O 2002 Anodic materials for rechargeable Li-batteries *J. Power Sources* **105** 151–60

[8] Li H, Shi L H, Lu W, Huang X J and Chen L Q 2001 Studies on capacity loss and capacity fading of nanosized SnSb alloy anode for Li-ion batteries *J. Electrochem. Soc.* **148** A915–22

[9] Mosby J M and Prieto A L 2008 Direct electrodeposition of CU_2Sb for lithium-ion battery anodes *J. Am. Chem. Soc.* **130** 10656–61

[10] Tarascon J M and Armand M 2001 Issues and challenges facing rechargeable lithium batteries *Nature* **414** 359–67

[11] Zhu J X *et al* 2010 Controlled synthesis of Sb nanostructures and their conversion to $CoSb_3$ nanoparticle chains for Li-ion battery electrodes *Chem. Mater.* **22** 5333–9

[12] Fransson L M L, Vaughey J T, Benedek R, Edstrom K, Thomas J O and Thackeray M M 2001 Phase transitions in lithiated Cu_2 Sb anodes for lithium batteries: an *in situ* x-ray diffraction study *Electrochem. Commun.* **3** 317–23

[13] Vaughey J T *et al* 2001 Structural and mechanistic features of intermetallic materials for lithium batteries *J. Power Sources* **97/8** 194–7

[14] Li L, Li G H, Zhang Y, Yang Y W and Zhang L D 2004 Pulsed electrodeposition of large-area, ordered Bi-1-Sb-x(x) nanowire arrays from aqueous solutions *J. Phys. Chem.* B **108** 19380–3

[15] Kumari L, Li W Z, Huang J Y and Provencio P P 2010 Nanosize transition metal antimonides, NiSb and $FeSb_2$: solvothermal synthesis and characterization *J. Phys. Chem.* C **114** 9573–9

[16] Xie J, Zhao X B, Mi J L, Tu J, Qin H Y, Cao G S and Tu J P 2006 Low-temperature solvothermal synthesis of $FeSb_4$42 nanorods as Li-ion batteries anode material *Electrochem. Solid State Lett.* **9** A336–9

[17] Yang X Y, Wang G M, Slattery P, Zhang J Z and Li Y 2010 Ultrasmall single-crystal indium antimonide nanowires *Cryst. Growth Des.* **10** 2479–82

[18] Burke R A, Weng X J, Kuo M W, Song Y W, Itsuno A M, Mayer T S, Durbin S M, Reeves R J and Redwing J M 2010 Growth and characterization of unintentionally doped GaSb nanowires *J. Electron. Mater.* **39** 355–64

[19] Lee Y H, Leu I C, Liao C L, Chang S T, Wu M T, Yen J H and Fung K Z 2006 Fabrication and characterization of Cu_2O nanorod arrays and their electrochemical performance in Li-ion batteries *Electrochem. Solid State Lett.* **9** A207–10

[20] Yan Q Y, Kim T, Purkayastha A, Ganesan P G, Shima M and Ramanath G 2005 Enhanced chemical ordering and coercivity in FePt alloy nanoparticles by Sb-doping *Adv. Mater.* **17** 2233–7

[21] Yan Q Y, Kim T, Purkayastha A, Xu Y, Shima M, Gambino R J and Ramanath G 2006 Magnetic properties of Sb-doped FePt nanoparticles *J. Appl. Phys.* **99**

[22] Portavoce A, Gas P, Berbezier I, Ronda A, Christensen J S, Kuznetsov A Y and Svensson B G 2004 Sb lattice diffusion in $Si_{1-x}Ge_x$/Si(001) heterostructures: chemical and stress effects *Phys. Rev.* B **69**

[23] Fang C W, Wu J M, Lee L T, Yeh H H, Wu W T, Lin Y H, Tsai P J and Chen Y R, Photocatalytic activity and electron field emission of necked ZnO:Bi nanowires *Electrochem. Solid State Lett.* **13** K63–6

[24] Lee J S, Brittman S, Yu D and Park H 2008 Vapor–liquid–solid and vapor–solid growth of phase-change Sb_2Te_3 nanowires and Sb_2Te_3/GeTe nanowire heterostructures *J. Am. Chem. Soc.* **130** 6252–8

[25] Zheng G F, Lu W, Jin S and Lieber C M 2004 Synthesis and fabrication of high-performance n-type silicon nanowire transistors *Adv. Mater.* **16** 1890

List of Figures

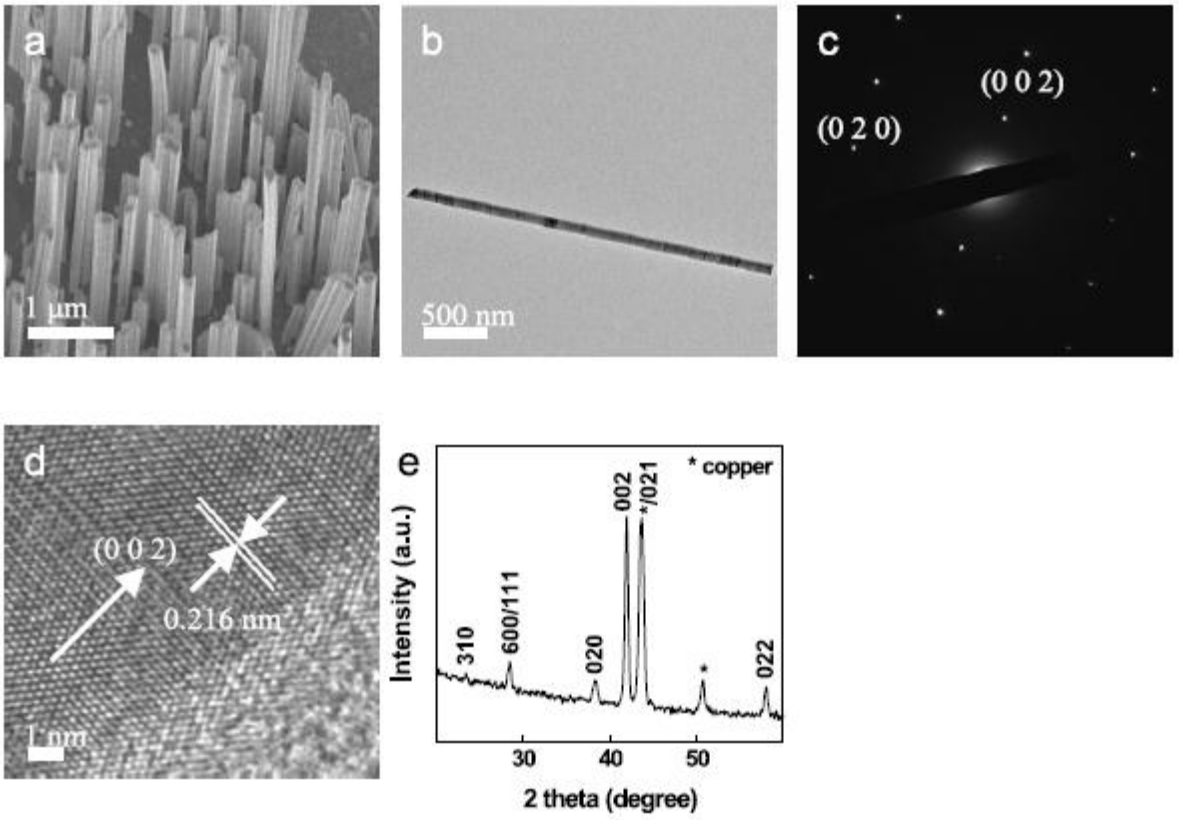
a
1 μm
b
500 nm
c
(0 0 2)
(0 2 0)
d
(0 0 2)
0.216 nm
1 nm
e
* copper
002
*/021
600/111
310
020
022
Intensity (a.u.)
30
40
50
2 theta (degree)

Figure 1

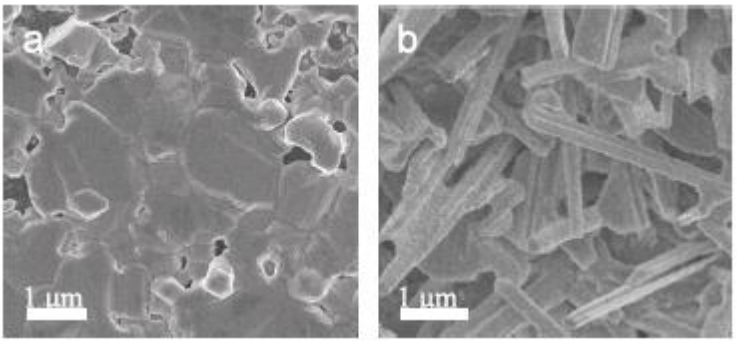

Figure 2

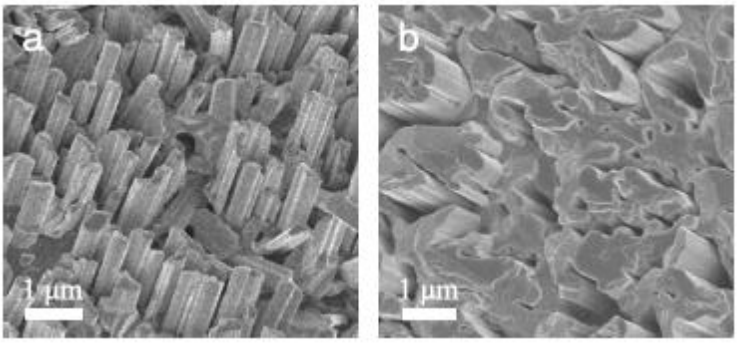

Figure 3

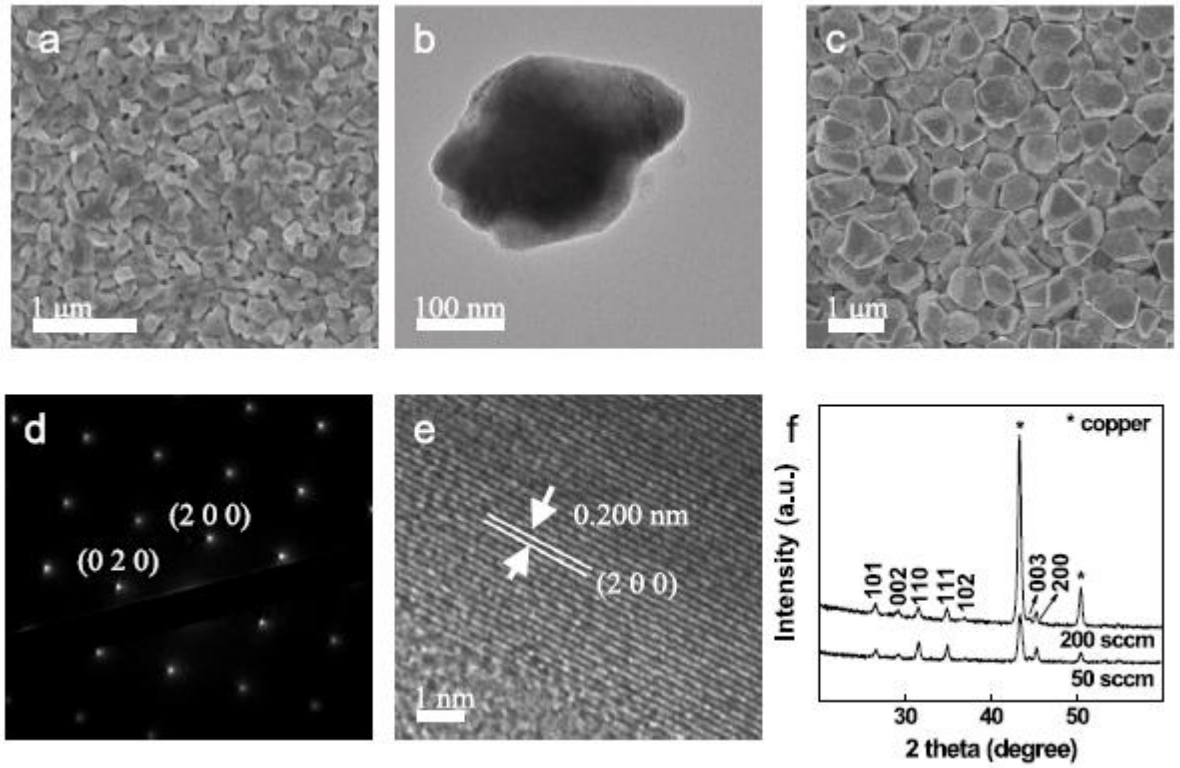
a
1 μm
b
100 nm
c
1 μm
d
(2 0 0)
(0 2 0)
e
0.200 nm
(2 0 0)
1 nm
f
* copper
Intensity (a.u.)
101
002
110
111
102
003
200
200 sccm
50 sccm
30
40
50
2 theta (degree)

Figure 4

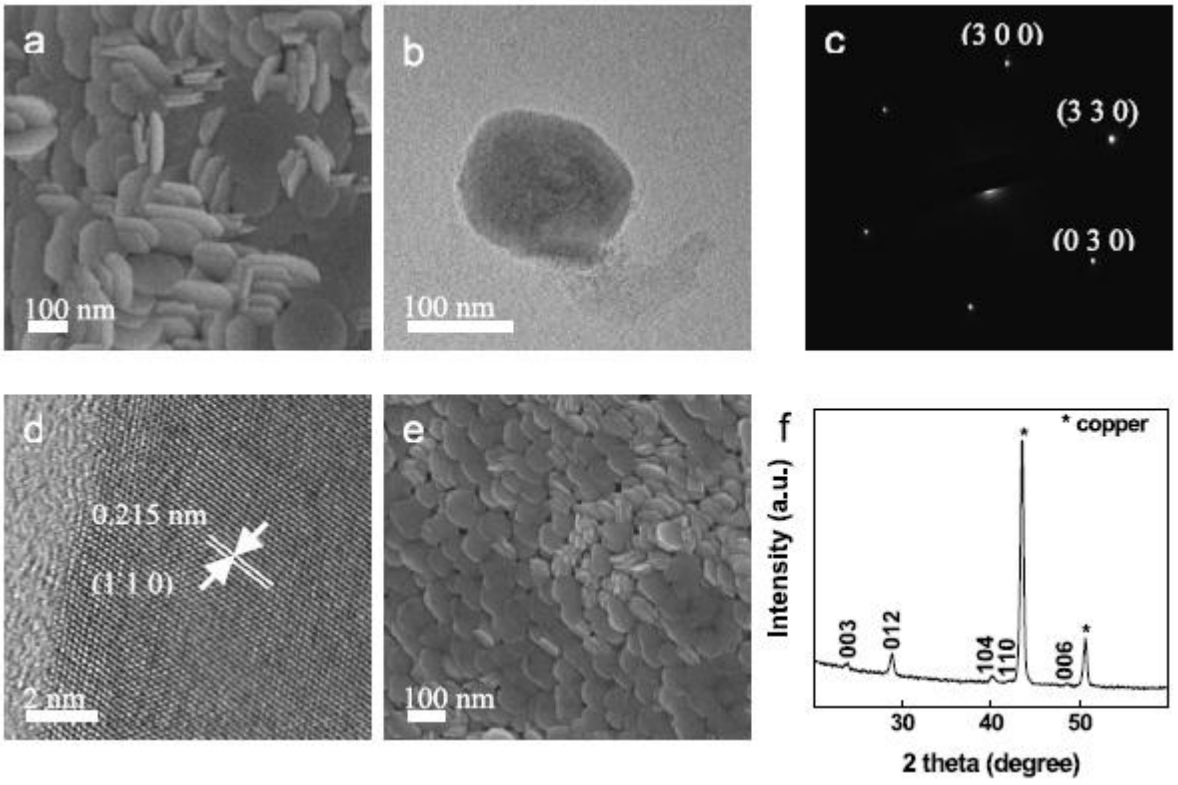
a
100 nm
b
100 nm
c
(3 0 0)
(3 3 0)
(0 3 0)
d
0.215 nm
(1 1 0)
2 nm
e
100 nm
f
* copper
Intensity (a.u.)
003
012
104
110
006
30
40
50
2 theta (degree)

Figure 5

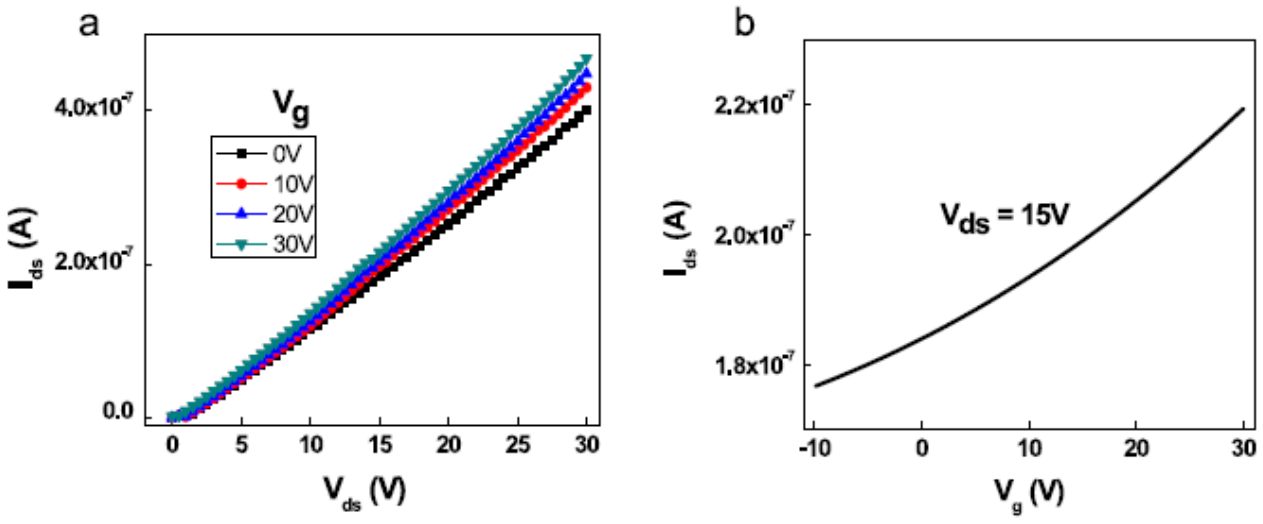
a
V_g
0V
10V
20V
30V
I_{ds} (A)
4.0x10^{-7}
2.0x10^{-7}
0.0
0
5
10
15
20
25
30
V_{ds} (V)
b
V_{ds} = 15V
I_{ds} (A)
2.2x10^{-7}
2.0x10^{-7}
1.8x10^{-7}
-10
0
10
20
30
V_g (V)

Figure 6